Civil and Environmental Engineering
Vol. 0, Issue 0, DOI: 10.2478/cee-2026-0079

Mechanistic Insights into the Long-term Sulphate–chloride Co-exposure Resistance of Self-compacting Engineered Cementitious Composites

Mohammed SHAKER AMOURI[1,*], Nada MAHDI FAWZI[1]

[1] Civil Engineering Department, University of Baghdad, Baghdad, Iraq.

[*] corresponding author: mohammed.amori2001m@coeng.uobaghdad.edu.iq

Date of Submission: 04 November 2025
Revision Date: 01 December 2025
Date of Acceptance: 12 December 2025

Civil and Environmental Engineering
Journal of the Faculty of Civil Engineering | University of Žilina

Abstract

This study elaborate on the collective impact of simultaneous sulphate–chloride ingress, cyclic wetting–drying and crystallization-induced microcracking, in the long-term degradation of concrete infrastructures in marine-like exposure conditions. This paper offers a comprehensive mechanistic assessment of the durability of self-compacting engineered cementitious composites (SC-ECC) exposed to sulphate, chloride, and combined sulphate–chloride exposure under a partial-immersion condition for 270 days. The developed blended SC-ECC having Class F fly ash and 1.5 vol% PVA fibres was evaluated by compressive strength, water and Rapid chloride penetration (RCPT) tests, half-cell potential (HCP) and scanning electron microscopy (SEM) analyses. At elevated sulphate concentrations, progressive but controlled degradation was observed from the experimental results. Water penetration was low (≤2.0 mm at 7.5% Na_2SO_4 after 270-days) suggesting that limited pore coarsening occurred even with microcrack generation. Across all regimes, the RCPT values remained ≤ 1500 C, further establishing the low ionic conductivity properties of SC-ECC compared with typical high-performance concrete with a similar exposure (Fig. 12). The most aggressive sulphate condition saw compressive strength retained about 80% of its water-cured reference even at 270 days. The measured corrosion potential (HCP) measurements (−120 to −430 mV vs. CSE) indicated low to moderately passive corrosion risk under chloride-only and sulphate-only exposures but more negative shifts were only developed under combined sulphate−chloride attack. SEM observations demonstrated a mechanistic degradation pathway driven by ettringite/gypsum crystallization in microcracks and ITZ widening, leading to enhanced ionic connectivity but not significant global porosity. Results corroborated from mechanical, transport, electrochemical, and microstructural aspects emphasize the excellent restrained resistance of fibered SC-ECC over long-term multi-ion, which exemplifies its high applicability for coastal and partially submerged structural use.

Keywords

Sulphate–chloride co-exposure; Durability performance; Corrosion resistance; PVA fibre reinforcement; Marine infrastructure.

1. Introduction

Concrete structures exposed to marine and hydraulic conditions are continuously subjected to the chemical and mechanical degradation processes due to the aggressiveness of the ambient conditions. The three-way interaction coupled with dynamic tidal wetting–drying (Tang et al., 2022), and hydrodynamic forces, constitute the early initial degradation as often expressed as microcrack propagation, leading to loss of alkalinity, delays of steel depassivation and reduction in long-term load-bearing capacity (Chen, 2024; Liu et al., 2017; Mousa et al., 2025). Degradation

pathways must be therefore carefully considered for coastal and offshore infrastructure where durability informs structural safety and maintenance sustainability under incidences of dual-ion exposures (Tian et al., 2025) which are known to be more destructive than their individual exposure regimens.

Regarding Engineered Cementitious Composites (ECC) ECC have been studied extensively as an impactful new high performance material family for harsh environments. Due to their inherent strain-hardening characteristic and microcrack widths being well defined (<100 μm), they provide a significant hindrance to ion transport (Odeyemi et al., 2025; Liu et al., 2017; Al-Masraf et al., 2024); they promote self-healing; and they increase the resistance of the composite to chemical attack. Although recent studies have demonstrated that ECC could perform better than conventional concrete in sulphate- or chloride-dominated environments, systematic long-term studies under combined sulphate–chloride exposure are still rare, especially with respect to their mechanistic microstructural evolution (Zhang et al., 2023; El Inaty et al., 2023). Parallel advances in self-compacting concrete (SCC) technology have enabled the development of flowable, non-segregating mixtures with excellent deformability, rheological stability, and enhanced placement characteristics (Ghanem and Awad, 2024; Al-Awadi & Fawzi, 2017; Al-Galawi and Ahmad, 2014). Recent rheology-based mix-design studies further demonstrated that optimizing particle packing and viscosity improves overall workability and mechanical performance (Narayana Rao & Kumar, 2023). Building on these developments, Self-Compacting ECC (SC-ECC) has recently been introduced as a novel class of fibre-reinforced, highly flowable composites that combine the rheological advantages of SCC with the ductility and crack-control mechanisms of ECC (Amouri & Fawzi, 2025).

Although SC-ECC exhibits promising fresh and mechanical properties, its long-term durability under realistic multi-ion conditions has not been adequately addressed in existing literature.

Research Gap

Despite extensive research on ECC durability, major gaps persist regarding:

1. The long-term performance of SC-ECC under combined sulphate–chloride co-exposure, particularly under partial-immersion regimes that simulate tidal marine conditions.
2. The mechanistic linkage between microstructural transformations (e.g., ITZ widening, ettringite/gypsum crystallization, fibre–matrix debonding) and measured durability indicators, such as permeability, chloride transport, and corrosion potential.
3. The absence of integrated mechanical–transport–electrochemical assessments for SC-ECC over extended exposure periods.

Research Significance and Impact

This work presents the first full mechanistic study of SC-ECC after extended dual-ion sulphate–chloride exposure sulphate–chloride exposure. To gain a better understanding of the degradation mechanisms relevant for long-term performance, the experimental program combines mechanical testing, transport properties, electrochemical characterization and SEM-based microstructural assessment. These results provide a basis for practical guidance for the design of durable SC-ECC mixtures for marine, tidal-zone and underwater structures, contributing to the sustainable construction of corrosion-resistant infrastructure.

2. Methodology

2.1. Research Design

The binary binder system used for the design of the SC-ECC mixture consisted of Ordinary Portland Cement (CEM I; IQS 5:2019) and Class F fly ash (ASTM C618), and the fine aggregate used was natural river sand (Zone II; IQS 45:1984). An amount of 1.5vol of 8–11mm polyvinyl alcohol (PVA) fibres was added to provide strain hardening behaviour and microcrack control, while a superplasticizer (polycarboxylate ether, according to ASTM C494 Type F) at a dosage of

1.75% of binder mass was used to achieve sufficient flowability. All mixing and curing were done using ASTMC192 potable water.

Mix proportions (per cubic meter) included: cement 650 kg, fly ash by 195 kg, sand by 570 kg, and water by 270 kg, which gave an effective water-to-binder ratio of 0.32. This composition yielded a stable, fibre-rich, self-compacting matrix with a high fibre dispersion suitable for subsequent durability assessment.

2.2. Materials and Procedures

SC-ECC mixtures were manufactured from a laboratory pan mixer, following in a standard processing order to assure homogeneous mixing of the binder, sand, superplasticizer, and subsequently PVA fibres. The test materials for composition mix were pre-mixed in dry form and then water with the necessary dosage of superplasticizer was added to achieve a homogeneous, self-compacting matrix. Fibers were added slowly to ensure a homogeneous distribution without clumping. The mixtures were mortar type ECC (without coarse aggregate) with high deformability and rheological stability. EFNARC (2002) limits for self-compacting composites were satisfied by fresh-state properties of 240–260 mm slump flows, 8–12 s V-funnel times, and 0.85–0.90 L-box ratios. A cohesive response between flow and cohesion under the optimised composition, which included Class F fly ash, 1.5 vol% PVA fibres and a polycarboxylate-based superplasticiser.

To ensure that the selected mixture was viable mechanically, direct tensile tests were performed on JSCE dog-bone specimens, showing evident strain-hardening and formation of multiple microcracks (<100 μm; more details are provided in ref.39). This confirmed that it was an appropriate Engineered Cementitious Composite (ECC) for further long-term sulphate–chloride exposure tests.

(a)

(b)

Figure 1: Dog-bone specimens of SC-ECC mixtures under direct tensile test: (a) specimen mounted in the testing machine during loading, and (b) specimen after failure showing the final dominant crack and residual fine cracks within the gauge length

2.3. Mixing Procedure

The SC-ECC mixture was prepared in a 30-L laboratory pan mixer under a controlled and reproducible mixing regime. The procedure was standardized as follows:

1. Dry mixing. Cement, Class F fly ash, and sand were first blended for 2 minutes at low speed to ensure uniform distribution of powders.

2. Addition of water and superplasticizer. Mixing water premixed with the required dosage of PCE-based superplasticizer was added gradually over 30–40 seconds while the mixer operated at low speed. The mixture was then allowed to blend for 1.5 minutes at medium speed until a uniform mortar consistency was achieved.

3. High-shear dispersion phase. After initial homogenization, the mixer was switched to high speed for 45–60 seconds to promote complete wetting of solids and stabilisation of the matrix rheology.

4. Fiber incorporation. The mixer was set to medium speed again, and then PVA fibres (1.5 vol%) were added slowly and continuously through a thin trickle avoiding fibre balling. The mixture was blended for 2 minutes at 1500 RPM followed by 1 minute at 700 RPM until full homogeneity and uniform fibre dispersion was observed.

5. Final verification. The total mixing time was approximately 7–8 minutes.

The mixture was inspected to ensure:

- No fibre clumping.
- Stable viscosity.
- Uniform colour.
- Proper mortar cohesiveness.

This detailed procedure ensures full reproducibility of the SC-ECC mixing process across different laboratories, addressing the reviewer's concern regarding technological transparency.

2.4. Fresh Density and Air Content

The fresh density of the SC-ECC mixture was determined following ASTM C138 using a calibrated density container of known volume. As soon as the concrete mix was prepared, the container was filled in one go without rodding or vibration, to avoid disturbing fibre distribution. Mass of the full container was weighed, and the fresh density was determined as follows:

$$\rho\_fresh = \frac{(M\_container+mix - M\_empty\ container)}{v} \quad (1)$$

Where:
ρ_fresh - fresh density of the SC-ECC mixture (kg/m^3),
M_container + mix - mass of the density container filled with fresh SC-ECC (kg),
M_empty container — mass of the empty density container (kg),
V - calibrated internal volume of the density container (m^3).

The measured fresh density of the optimized SC-ECC mix was 2110 ± 25 kg/m^3, indicating a dense, fibre-stabilized matrix with minimal entrapped air. Correspondingly, the air content, obtained by comparing measured and theoretical density, was approximately 2.0 ± 0.3 %, consistent with the expected range for PVA-reinforced ECC systems.

2.5. Data Collection

All specimens were cast using the validated SC-ECC mixture and placed without vibration to preserve the self-compacting characteristics and prevent fibre segregation. After demolding at 24 ± 2 h, all samples were moist-cured at 20 ± 2 °C for 28 days. Fragments from compressive specimens were later used for SEM examination.

Following curing, specimens were exposed under partial-immersion conditions to replicate tidal wetting–drying cycles. Three chemical environments were considered:

- Chloride solution: 3% NaCl by weight of water.
- Combined sulphate–chloride solution: 2.5%, 5.0%, and 7.5% Na_2SO_4, each combined with 3% NaCl.
- Sulphate solution only: 2.5%, 5.0%, and 7.5% Na_2SO_4.

Durability performance testing consisted of water permeability, half-cell potential, and compressive strength tests and was performed on all exposure regimes except for water permeability and rapid chloride penetration (RCPT ASTM C1202) which were only assessed on the sulphate-only specimens. RCPT was conducted at 56 days of exposure to ensure comparison consistency with the reference group. The exposure duration was 270 days, and the data were

collected at 90, 180 and 270 days. To keep ion concentrations stable, they renewed the solutions every 30 days. The partial-immersion configuration supported natural damage processes through cyclic wetting–drying and crystallization of the salt near the evaporation front.

The program for assessing damage reactions was employed for a thorough assessment of the mechanical, electrochemical, transport, and microstructural responses of SC-ECC when subjected to sulphate–chloride attack. The sequence of the experimental process is outlined in a flowchart in Figure 2.

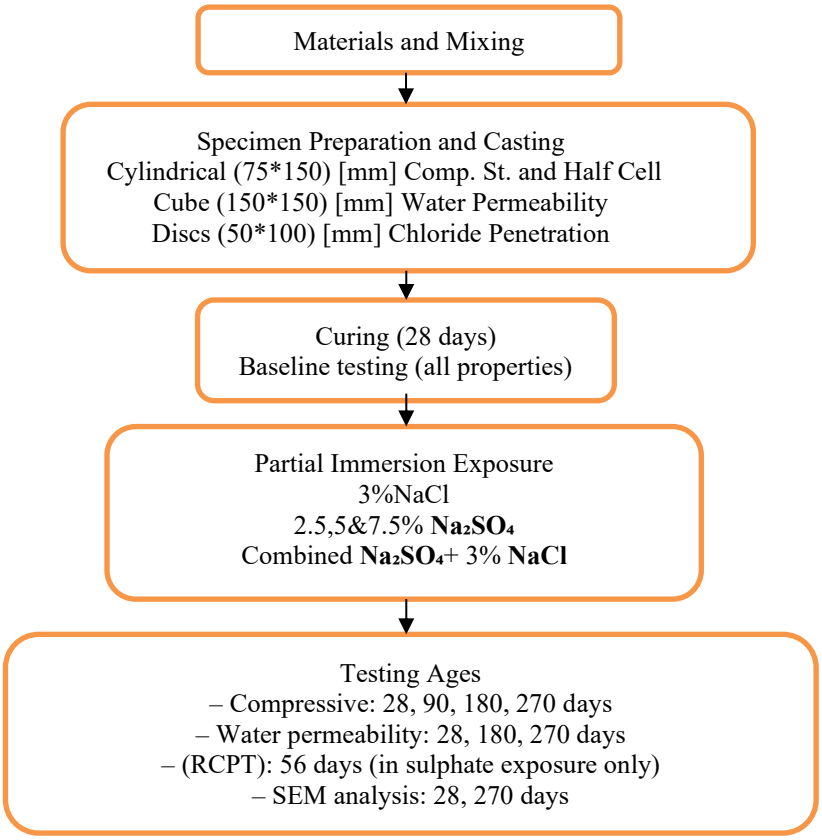

Figure 2: The experimental program of flowchart summarizing sequence for SC-ECC mixtures, including material selection, specimen casting, curing regime, exposure conditions, and testing schedule. The chart outlines the chronological stages—from material preparation

3. Testing Methods

A comprehensive testing program was conducted to evaluate the mechanical, transport, and electrochemical performance of the SC-ECC mixtures under sulphate, chloride, and combined sulphate–chloride exposure. All tests were performed in accordance with the relevant international standards. The following subsections summarize the procedures used to assess compressive strength, permeability, chloride penetration, half-cell potential, and microstructural characteristics.

3.1. Compressive Strength

Compressive strength was measured on cylindrical specimens (75 × 150 mm) in accordance with ASTM C39/C39M using a 2000 kN servo-hydraulic testing machine. A loading rate of 0.25 MPa/s was applied, and three replicates were tested for each exposure condition at 90, 180, and 270 days. The mean value of the three measurements was taken as the representative compressive strength for each regime.

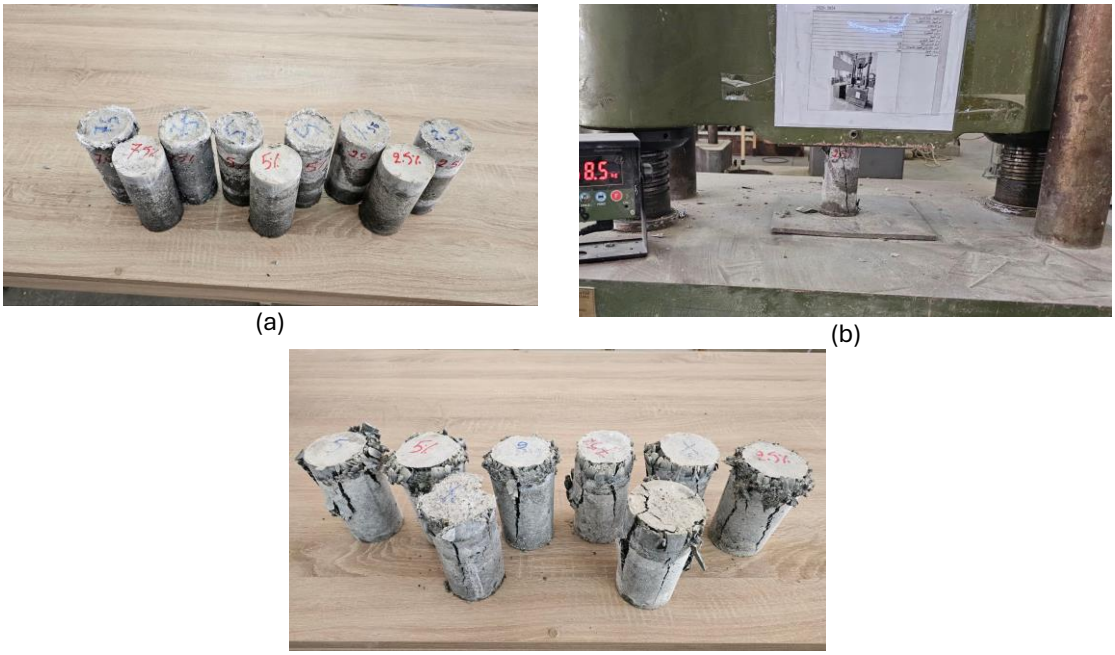

Figure 3: Compressive strength testing of SC-ECC specimens: (a) specimens after long-term exposure before testing, (b) experimental setup during compressive loading, and (c) post-failure appearance exhibiting gradual crushing and limited fragmentation, indicative

3.2. Water Permeability

Water permeability was evaluated according to EN 12390-8 (2019) using 150 × 150 × 150 mm prismatic specimens subjected to a constant hydraulic pressure of 0.5 MPa for 72 h. After testing, each specimen was split along its central axis, and the maximum penetration depth was measured using a digital caliper with 0.01 mm accuracy. The results were interpreted following the classification procedure of DIN 1048-5 (1991). Measurements were conducted at 90, 180, and 270 days for the corresponding exposure regimes.

Figure 4: Water permeability test setup for SC-ECC specimens under 0.5 MPa hydrostatic pressure, results evaluated according to DIN 1048-5 (1991)

3.3. Chloride Penetration

Chloride penetration was evaluated using the rapid chloride penetration test (RCPT) in accordance with ASTM C1202 (2022). Disc-shaped specimens (100 mm diameter × 50 mm thick) were prepared and preconditioned through vacuum saturation following the standard procedure. Testing was performed after 56 days of exposure to Na_2SO_4 solutions with concentrations of 2.5%, 5.0%, and 7.5%, and compared with water-cured reference specimens.

A constant potential of 60 V DC was applied for six hours across each specimen, and chloride-ion penetrability was quantified based on the cumulative charge passed (Coulombs). Classification of penetrability levels followed the criteria provided in ASTM C1202.

Table 1: Chloride penetration classification based on total charge passed. ASTM C1202 (2022)

Total charge passed (Coulombs)	Chloride penetration classification
>4000	High
2000-4000	Moderate
1000-2000	Low
100-1000	Very low
<100	Negligible penetration

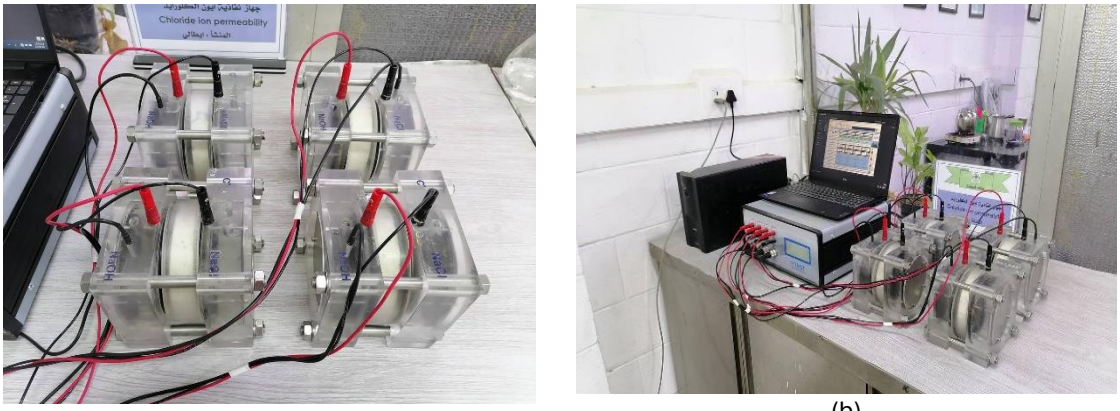

(a) (b)

Figure 5: Rapid chloride penetration testing of SC-ECC specimens: (a) specimen preparation and surface sealing of 100 × 50 [mm] cylindrical discs before testing, and (b) data acquisition and monitoring of the total charge passed through the specimens

3.4. Half-cell Potential

Half-cell potential (HCP) measurements were conducted in accordance with ASTM C876-22a to evaluate the corrosion activity of the embedded steel reinforcement. Cylindrical specimens (75 × 150 mm) were cast with a centrally embedded 12-mm deformed steel bar, providing a 30-mm concrete cover and an effective embedment length of 75 mm.

A copper/copper sulphate reference electrode (CSE) was positioned on the specimen surface, and potentials were recorded at predefined measurement points using a high-impedance voltmeter at 90, 180, and 270 days. Interpretation of corrosion likelihood followed the ASTM C876 criteria, where potentials more negative than −350 mV indicate a high probability of active corrosion, values between −200 and −350 mV reflect uncertain probability, and values more positive than −200 mV correspond to passive conditions.

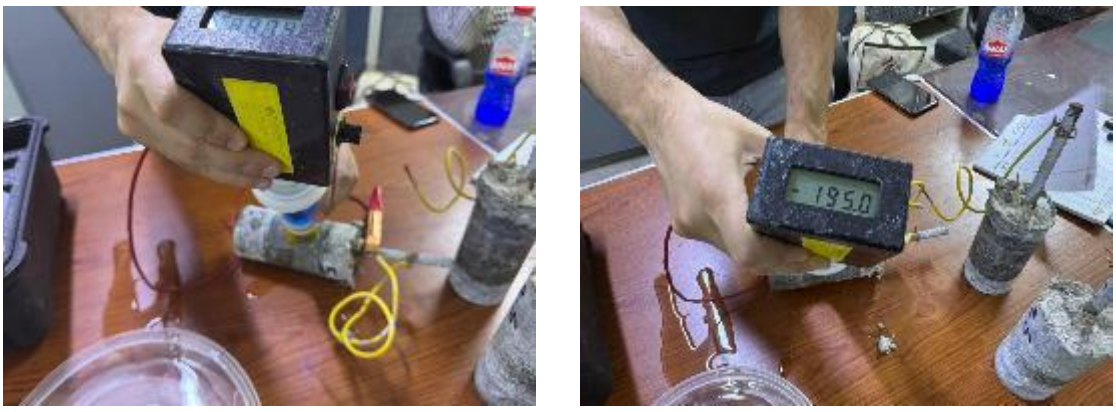

(a) (b)

Figure 6: Half-cell potential testing of SC-ECC specimens: (a) typical test setup showing electrode positioning and electrical connection on the specimen surface, and (b) measurement of corrosion potential using a $Cu/CuSO_4$ reference electrode (CSE)

3.5. Scanning Electron Microscopy (SEM)

Scanning electron microscopy (SEM) was performed on fragments obtained from failed compressive specimens to examine microstructural features after chemical exposure. Samples were oven-dried at 40 ± 2 °C, sputter-coated with a thin gold layer to ensure conductivity and imaged using a Thermo Scientific Axia ChemiSEM microscope. Observations were conducted at various magnifications using secondary (SE) and backscattered electron (BSE) modes under an accelerating voltage of 15 kV.

Micrographs were collected for specimens subjected to chloride, sulphate, and combined sulphate–chloride exposures to document the morphology of hydration products, microcrack patterns, and fibre–matrix interface characteristics.

4. Results

4.1. Long-Term Compressive Performance of SC-ECC under Sulfate and Sulfate–Chloride Exposure

Figure 7: Results of compressive strength of SC-ECC (conversion of results to equivalent cube strength (factor 1.25) The strength of all mixtures at 90 days corresponded to continued hydration as well as the pozzolanic activity of Class F fly ash which densified the matrix and optimized particle packing [Hotz, H., Götz, W., Schönfeld, M. and Vögtle, T. (2006). In recent decades, numerous in-situ developments have confirmed that the principle of optimal material distribution prevails in concrete. It was particularly pronounced for the water-cured and chloride-only specimens, both of which exceeded 125% of their 28-day control strength at 180 days. As all the hydration products remain undisturbed by chloride ions, thus the developing matrices are densified similarly to reference curve, chloride ions are not known to hinder the mechanisms of decomposition through weathering.

However, the rate of strength gain was significantly reduced under sulphate attack. Some slight short-term (< 180 days) enhancement was still noted - especially due to the dense low penetration character of ECC, and the ongoing hydration of unreacted clinker - yet, the saturation gradient and progressive sulphate crystallization hindered densification at longer ages. All sulphate-containing regimes showed marked reductions in strength by 180 days or more. For the most aggressive environment examined (7.5% Na_2SO_4 + 3% NaCl), 270-day strengths from 180 days were retained at approximately 80%-which is consistent with microcrack propagation and ettringite/gypsum formation as detected using SEM imaging.

Residual strengths of the sulphate-only specimens were slightly greater than the dual-ion series, confirming the observed synergistic degradation induced by combined sulphate–chloride exposure. The effect of chloride ions plays a special role in accelerating the ionic transport process, while the expansion induced by sulphate can link microcracks and provide further ease for deeper penetration and increased deterioration rates. This coupling mechanism is consistent with the observations made by Tian et al. (2025) and El Inaty et al. (2023).

Cyclic wetting–drying, as well as crystallization at the evaporation front in the partial-immersion regime, exacerbated the deterioration by creating local stress concentrations leading to surface microspalling. On the contrary, the reference SC-ECC remained stable with a further increase up to 270 days (≈150% of its 28-day value), emphasizing the intrinsic stability and capacity of the matrix for further refinement in the absence of competitive ions.

In all exposure conditions, SC-ECC presented significant residual compressive capacity that was consistently lower than strength losses typically reported for conventional concretes. The results emphasize that sulphate exposure can may allow for some early-age strength gain, however, subsequent microcracking from crystallization far outweighs the initial benefits due to bulk porosity increase, causing overall long-term deterioration beyond 180 days.

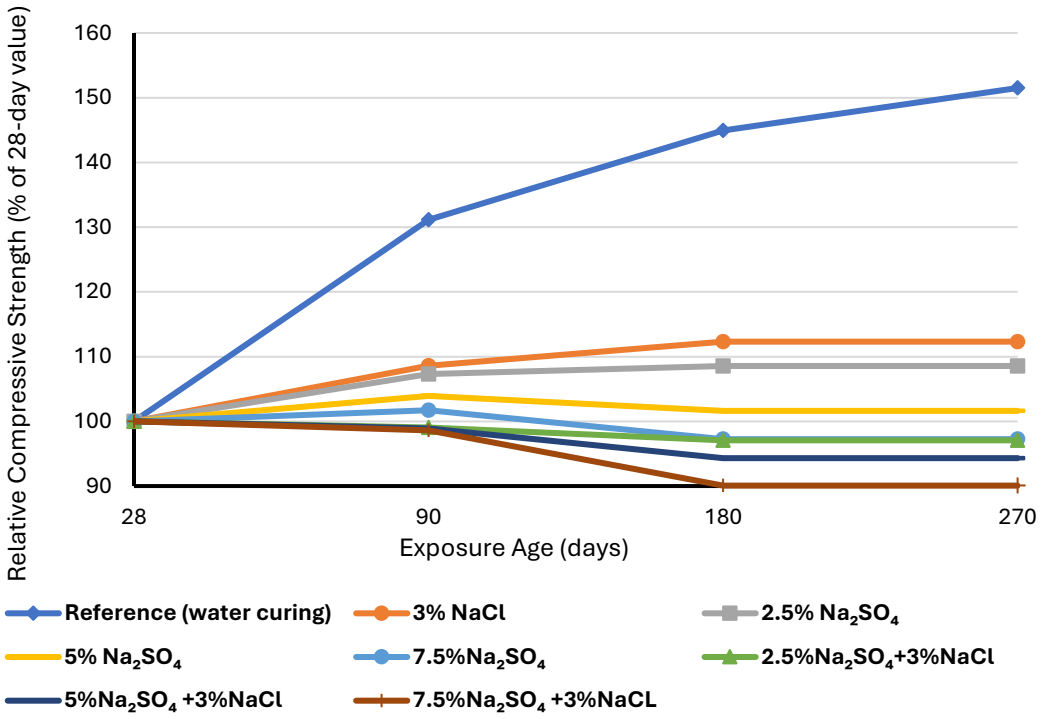

Figure 7: Relative compressive strength development of SC-ECC specimens under chloride-only, and combined chloride–sulphate exposure at 28, 90, 180, and 270 days (normalised to 28-day values = 100 %)

4.2. Evolution of Water Permeability under Sulphate-Induced Microstructural Degradation

As presented in Figure 8, the water permeability results reveal that SC-ECC maintained an extremely low penetration depth (<0.6 mm) at 28 days, which reflects the dense matrix achieved through the synergistic effect of Class F fly ash and homogeneously dispersed PVA fibres. Hydraulic transport was, at the reference age, effectively limited by the fine capillary system and the microcracks bridged by fibres.

Over time frames that corresponded to later ages, the evolution of permeability was shown to depend increasingly on sulphate concentration. The penetration depth increased only marginally (≈ 0.69 mm at 270 days) for 2.5% Na_2SO_4, indicating that diffusion of low-concentration sulphate tends to be restricted to the surface layer without affecting internal continuity. On the contrary, 5% Na_2SO_4 exposure doubled the reference penetration depth, suggesting prompt microcrack activation and localized dissolution of both portlandite and some of the C–S–H framework.

The penetration was greater than the bottom and the most aggressive condition (7.5% Na_2SO_4) induced a clear increase in penetration with a maximum of approximately 1.9 mm at 270 days. This reaction is in line with sulphate-attack mechanisms in which ettringite and/or gypsum crystallize in pores and microcracks, exerting localized tensile stresses, and assisting crack–crack coalescence, especially at fibre-matrix interfaces. Post-permeability SEM (Section 3.5) confirms this mechanism by the observation of microcrack branching and ITZ deterioration that correspond with the increased permeation.

The exposure area subjected to partial-immersion accelerated the degradation by repeated wetting–drying and salt recrystallization around the evaporation front. Thus, these cycles were instrumental in initial subsurface pore coarsening and development of a shallow zone of microdamage, consistent with the mechanistic trends reported in El Inaty et al. (2023) and Tian et al. (2025). Importantly, the increase of the permeability did not accompany bulk porosity change but reflects more the emergence of discrete microcrack behaviour like sulphate expansive reactions.

Over these conditions, penetration depths were still very low (<2 mm even with the highest concentration and 270 days). The values are far below the 5-10 mm reported for high performance concretes for the same exposures and

show much higher transport resistance of SC-ECC. The combined effect of dense matrix, fly-ash driven refinement and stable fibre-bridged microcrack widths contributed to the maintained matrix continuity, consistent with sustained compressive performance (Section 4.1.).

In conclusion, these results confirm that permeability evolution due to sulphate concentration governs permeability evolution, and that the SC-ECC system remains an efficient barrier to fluid transport. This shallow penetration depths again emphasize that degradation is primarily a surface-governed and microcrack driven mechanism instead of reflecting deep matrix softening.

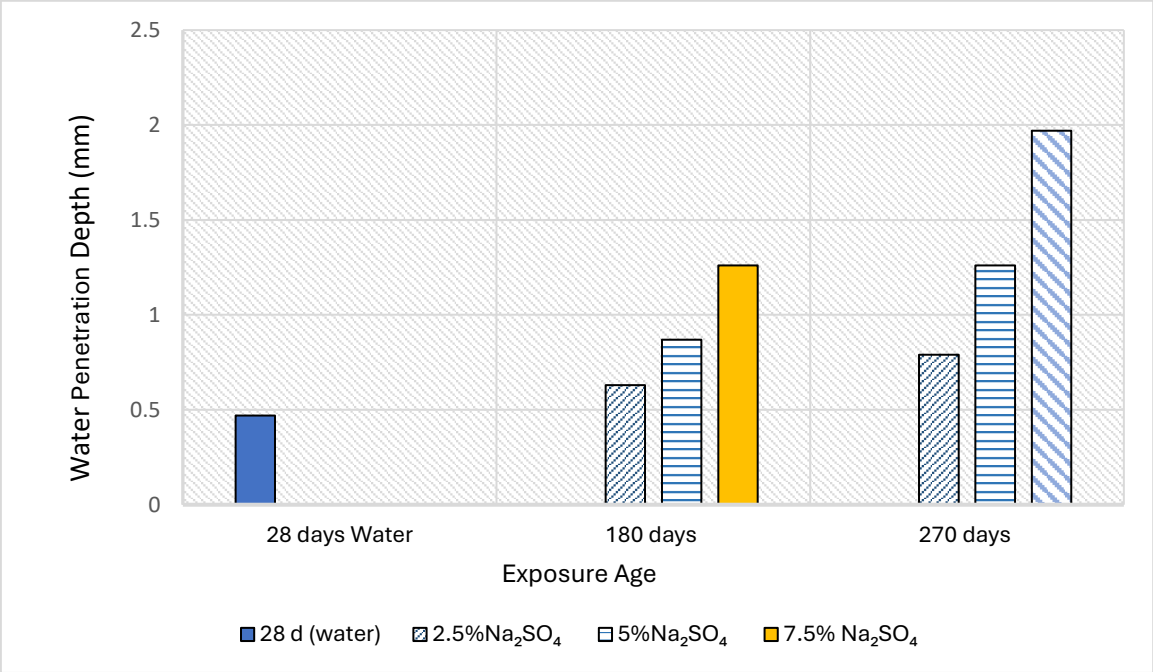

Figure 8: Water penetration depth of SC-ECC specimens exposed to different sulphate concentrations (2.5 %, 5.0 %, and 7.5 % Na_2SO_4) at 28, 180, and 270 days under partial-immersion conditions. Each value represents the mean of three specimens

4.3. Mechanistic Evaluation of Chloride Transport under Sulphate-induced Matrix Damage

The RCPT results after 56 days of sulphate exposure revealed a clear dependence of chloride-ion transport on sulphate concentration (Table 2, Figure 9). Water-cured reference specimens showed very low charge passage (663–750 C), corresponding to the "very low" ASTM C1202 (2022) category. The explanation for this behaviour is that dense structure provided by fly-ash-driven matrix refinement and stable (fibre-bridged) microcracks together restrict the formation of continuous ionic pathways.

Charge passage increased gradually under 2.5% Na_2SO_4 (817–983 C) to 7.5% Na_2SO_4 (1012–1349 C) with rising sulphate concentration. Notably, this increase is not a rise in total pore volume, but rather, microstructural changes because of ettringite and gypsum formation. These expansive products create local tensile stresses that generate microcracks within the matrix and across the PVA/matrix interfacial transition zone (ITZ) in microscale. These microdefects enhance the electrical connection between the pores, which accelerates the ionic transport while maintaining a dense bulk matrix - in agreement with the SEM observations and mechanistic explanation by Tian et al. (2025) and El Inaty et al. (2023).

The enhanced transport of charge at the highest sulphate concentration may imply partial fibre–matrix bonding degradation and local debonding at the ITZ. When microcracks propagate above the intrinsic self-healing ability of the SC-ECC, isolated pores are interconnected leading to the formation of continuous pathways for electrical conduction. ECC has been reported previously (Liu et al., 2017; Şahmaran et al., 2008) to show increased RCPT values without detectable mechanical degradation, which further showed that RCPT is controlled mainly by the electrical continuity, not by the penetration depth of Cl^- as it also has a significant role with specimens with a high RCPT value.

Despite the sulphate-induced increases, all SC-ECC mixtures maintained total charges below 1500 C—well within the "low" penetrability category and markedly lower than the >2500 C typically reported for high-performance concretes exposed to comparable sulphate conditions. This sustained resistance reflects long-term pozzolanic consumption of $Ca(OH)_2$ and the continued effectiveness of fibre bridging in controlling crack width, even under partial immersion. Although wetting–drying cycles likely increased ionic mobility near the evaporation front, the overall transport resistance remained high.

Overall, the results indicate that chloride transport under sulphate exposure is dominated by microcrack evolution and enhanced interfacial conductivity rather than significant pore coarsening. Consequently, RCPT serves as a diagnostic indicator of microstructural stability under coupled sulphate–chloride attack, complementing the permeability and strength trends observed in Sections 4.1 and 4.2.

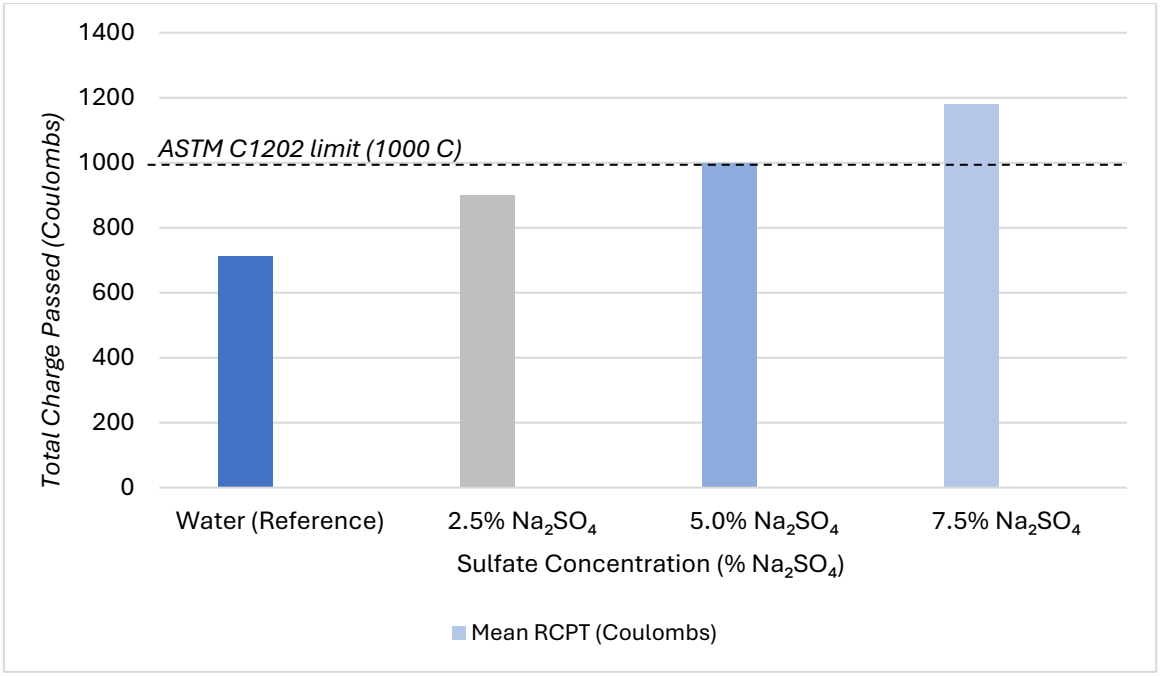

Figure 9: Rapid chloride penetration (RCPT) results of SC-ECC specimens under different sulphate concentrations (2.5–7.5 % Na_2SO_4) at 56 days. Each value represents the mean of three specimens. The dashed line denotes the ASTM C1202 limit for "very low" chloride Penetration (1000 C)

4.4. Mechanistic Interpretation of Half-cell Potential Response in SC-ECC under Multi-ion Attack

The half-cell potential (HCP) trends of SC-ECC under chloride, sulphate, and combined sulphate–chloride exposure are shown in Table 2 and Figure 10. Water-cured specimens maintained stable potentials between − 118 and −128 mV (CSE), indicating a passive steel state and confirming that the dense, fly-ash-rich SC-ECC matrix preserves alkalinity in non-aggressive environments.

Under sulphate-only exposure (2.5–7.5% Na_2SO_4), potentials gradually shifted toward more negative values (≈ −170 to −252 mV at 270 days). This moderate depolarization reflects partial portlandite consumption and the development of near-surface microcracks driven by ettringite/gypsum crystallization. Nevertheless, all sulphate-only results remained within the low-to-moderate corrosion-probability range of ASTM C876, indicating that the internal microstructure continued to restrict ionic mobility despite localized deterioration.

In contrast, exposure to chloride (3% NaCl) yielded a better-defined potential drop—from around −230 mV to −310 mV within 270 days—closer to the corrosion threshold for active corrosion (−430 mV at 270 days, which was above the high-probability corrosion threshold. At lower sulphate concentrations (5% and 2.5% Na_2SO_4 + 3% NaCl) significant reductions were also seen (≈ −375 mV and −345 mV respectively). This behaviour is a result of two coupled mechanisms.

(i) depassivation of the reinforcing steel driven by chloride,

(ii) microcrack formation from sulphate expansion, that widen ionic transport pathway.

The mechanistic interaction shown both by RCPT trends (Section 4.3) and SEM evidence (Section 3.5), is what ultimately explains why under direct exposure to dual-ions a sharper potential drop was observed compared to either ion alone. On the microstructural level, chloride penetration creates microscopic anodic sites along the steel surface, and sulphate crystallization creates tensile stresses in the vicinity of the evaporation front, further promoting pore connectivity. During this partial-immersion regime, the cyclic wetting–drying characteristic continuously enhances these effects through successive dissolution and recrystallization cycles.

Although the additional probability of corrosion under combined attack conditions is more pronounced, the electrochemical resistance of SC-ECC was still higher than the corresponding measure of conventional concretes which are typically observed to have potentials more negative than −500 mV for the same exposure conditions (Song & Saraswathy, 2007). The elevated fly-ash content constrains Ca(OH)2 available [8], whereas PVA fibres impede crack propagation and consequently limit the spread of uninterrupted corrosion pathways [9]. Mechanistically, this behaviour suggests early corrosion initiation is dominated by chloride ions, whereas sulphate exposure governs the corrosion propagation process via microstructural degradation.

In general, the direct correspondence between trends in HCP and RCPT results demonstrates that there is a coherent mechanistic relationship between ionic migration and the electrochemical performance. Both persistency of multi-ion contacts and the evolution of near-surface cracking and moisture gradients over time are key findings from SC-ECC measurements, confirming the resistance of SC-ECC to extended multi-ion exposure while showcasing the sensitivity of HCP technique to convert corrosion activity into time-lapsed potential outputs rendering HCP not applicable to partially immersed systems.

Table 2: Half-cell potential results of SC-ECC specimens under different exposure regimes (values in mV vs. CSE; ASTM C876 classification shown in parentheses)

Exposure Condition	28 days mean (mV)	Corrosion risk classification (ASTM C876) @28d	90-day mean (mV)	Corrosion risk classification (ASTM C876) @90d	180 days (mV)	Corrosion risk classification (ASTM C876) @180d	270 days (mV)	Corrosion risk classification (ASTM C876) @270d
7.5% Na_2SO_4	−205	Moderate	−217	Moderate	−235	Moderate	−252.5	Moderate
5% Na_2SO_4	−184	Low	−196	Low	−210	Low/Moderate	−222.5	Moderate
2.5% Na_2SO_4	−170	Low	−182	Low	−195	Low	−207.5	Low/Moderate
7.5% Na_2SO_4 + 3% NaCl	−340	Moderate/High	−351	Moderate/High	−395	High	**−430**	**High/Very high**
5% Na_2SO_4 + 3% NaCl	−290	Moderate	−305	Moderate	−345	Moderate/High	**−375**	High
2.5% Na_2SO_4 + 3% NaCl	−270	Moderate	−285	Moderate	−317.5	Moderate	−345	Moderate/High
3% NaCl only	−230	Moderate	−248	Moderate	−277.5	Moderate	−310	Moderate **(Near high)**
Water (reference)	−118	Very Low	−118	Very Low	−122.5	Low	−127.5	Low

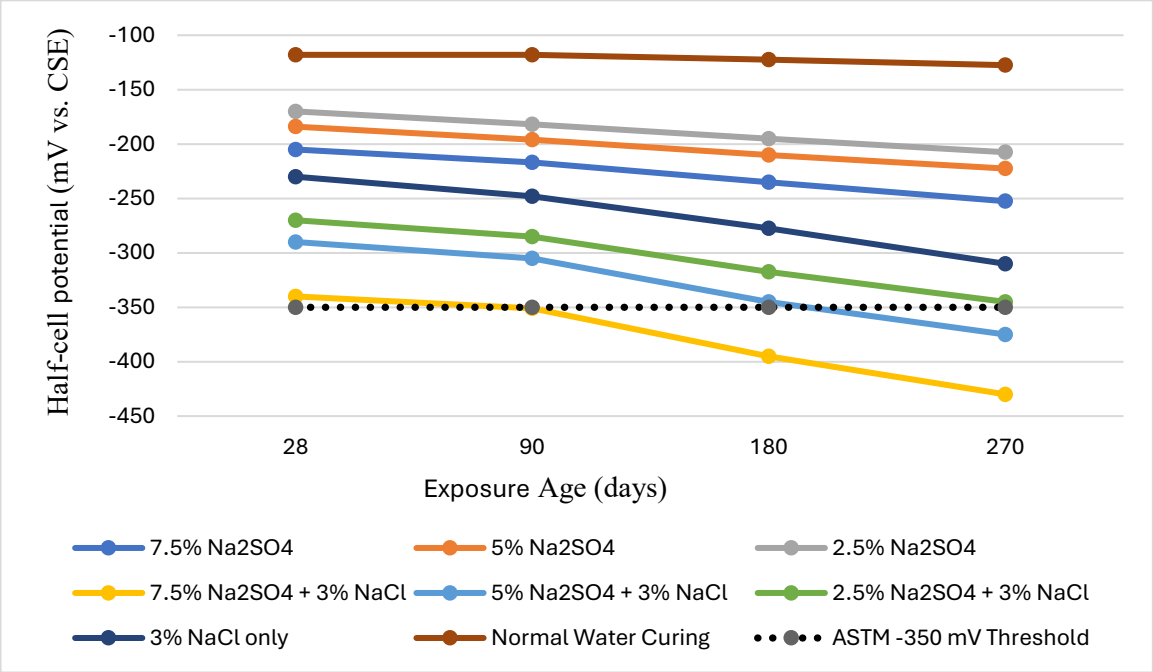

Figure 10: Development of half-cell potential of SC-ECC specimens under chloride-only, sulphate-only, and combined chloride–sulphate exposures up to 270 days. The dashed line at −350 mV denotes the ASTM C876 threshold for high corrosion probability

4.5. Microstructural observations and discussion

SEM observations in Figure 11 provide microstructural validation for the mechanical, transport, and electrochemical trends described in Sections 4.1–4.4. The evolution of the SC-ECC matrix under increasing sulphate concentrations reveals a transition from a dense, refined microstructure at early age to progressive microcracking, ITZ widening, and accumulation of sulphate-reaction products at later ages.

(a) Water-cured reference (28 days)

The reference microstructure exhibits a compact C–S–H matrix with limited portlandite, narrow ITZ regions, and strong bonding to PVA fibres. The absence of continuous capillary pathways is consistent with the extremely low permeability (<0.6 mm), low RCPT values, and passive HCP response. The uniformity of the matrix confirms the effectiveness of fly-ash-driven refinement and fibre dispersion.

(b) 2.5% Na_2SO_4 (initiation stage, 270 days)

Low-density ettringite formations appear near pores and ITZ zones, while the bulk matrix remains largely intact. Slight ITZ widening and isolated microcracks correspond to the marginal increase in penetration depth (~0.7 mm) and the modest RCPT rise. HCP values remain within the low/moderate corrosion-probability range, indicating sulphate reactions remain superficial under this concentration.

(c) 5% Na_2SO_4 (propagation stage, 270 days)

More distinctive ettringite aggregates and formation of gypsum plates appear in the finer void regions and in microcracks during early-stage crystal growth. The ITZ broadening (≈11–13 μm) signifies localized C–S–H disturbance and correlates with the observed increase in water ingress and higher RCPT (≈1000–1200 C) values. The microcrack connectivity is observed in HCP depolarization to −300 mV, which indicates the beginning of partial depassivation, is consistent (upper region).

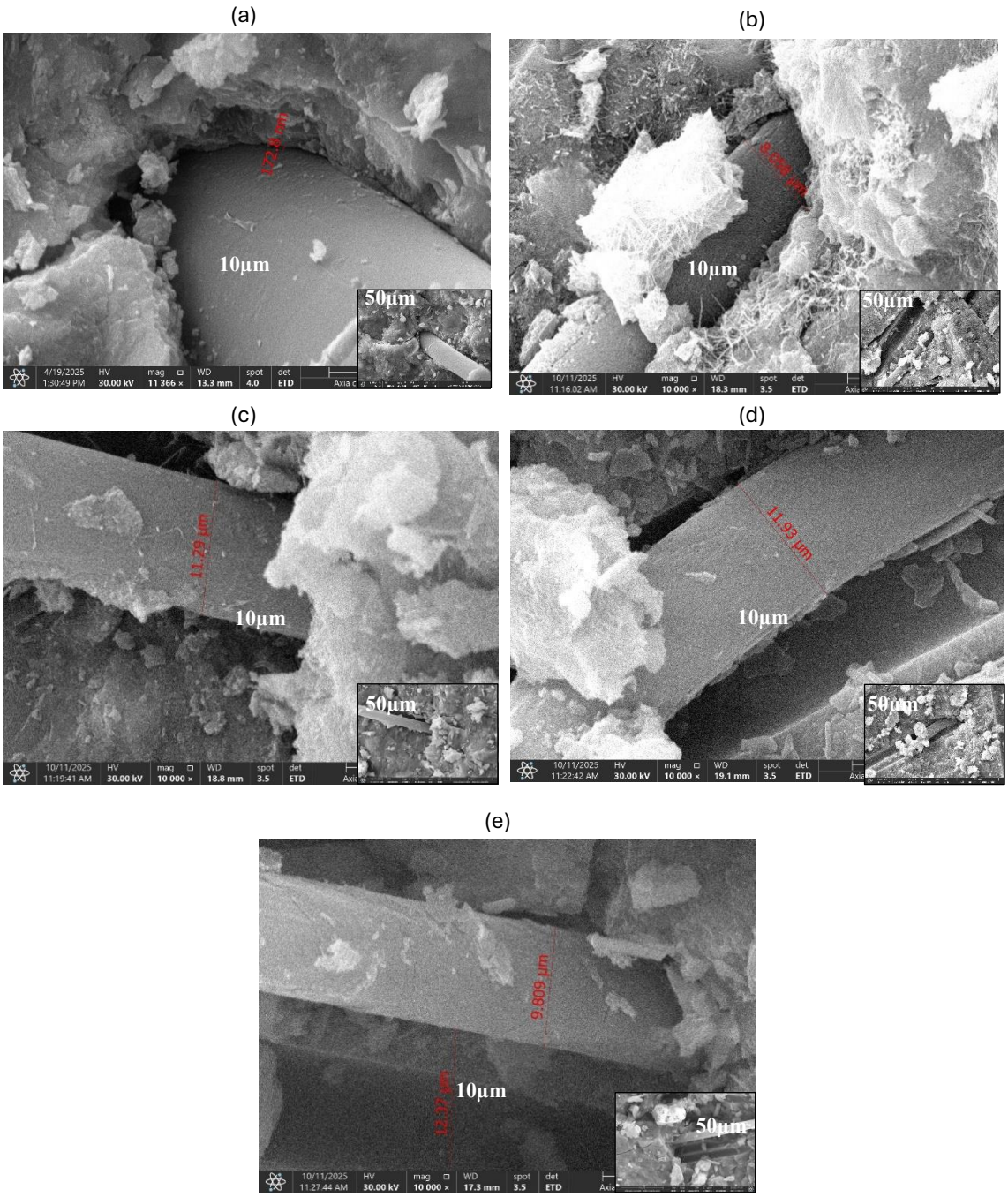

Figure 11: SEM micrographs of SC-ECC specimens showing microstructural evolution with sulphate concentration and exposure duration: (a) 28-day water-cured reference sample; (b) 2.5 % Na_2SO_4 — early ettringite nucleation near fibre–matrix interfaces; (c) 5 % Na_2SO_4 - denser ettringite and gypsum deposits causing local cracking; (d) 7.5 % Na_2SO_4 — severe matrix deterioration and widened ITZ; (e) high-magnification view of fibre–matrix interphase highlighting partial debonding and secondary deposition

(d) 7.5% Na_2SO_4 (advanced damage stage, 270 days)

High sulphate concentration generates large, interconnected microcracks, fibre debonding, and plenty of acicular ettringite and tabular gypsum between ITZs. However, this condition intensifies, leading to deeper penetration (1.9–2.0 mm), increased RCPT (1200–1350 C), and HCP < −350 mV caused by increased ITZ width (> 13 µm) and clear fibre pull-out. These trends confirm that sulphate-mediated expansion becomes the major degradation mechanism in the latter stages.

(e) Fiber–matrix interface response

High magnification imaging illustrates surface deposits and textured alterations on PVA fibres exposed to elevated sulphate concentrations. Despite little growth in bulk porosity through only weak partial debonding, this transition occurs from effective crack bridging to reduce fibre efficiency and thus increases ionic transport Retention of fibre bridging at the lower sulphate concentration is consistent with the increased compressive strength and better transport resistance.

Mechanistic Interpretation

Taken together, the SEM evidence indicates an advancing mechanism of sulphate-induced deterioration where ettringite initially nucleates at pore walls, then crystallizes within microcracks, creates internal tensile stress, and finally pulls apart the ITZ. These microstructural changes promote ionic connectivity which directly accounts for the observed increases in RCPT and the HCP response that is shifted negative. Immersion–drying: During single-side immersion, wetting–drying occurs cyclic near the evaporation front, enhancing dissolution–precipitation, which feeds a cracking → permeation → crystallization feedback loop.

These effects are countered, however, as fly-ash refinement and PVA-fibre bridging are still effective at hindering crack coalescence, retaining in SC-ECC RCPT ≤ 1500 C and ~80 % strength-retention under even the most aggressive conditions. This indicates that sulphate-dominated microcrack development is the controlling degradation mechanism, rather than bulk porosity change, and provides strong mechanistic insight for the coupled mechanical, transport, and electrochemical results shown in this study.

5. Conclusion

This study examined the long-term durability of SC-ECC under sulphate, chloride, and combined sulphate–chloride exposure through mechanical, transport, electrochemical, and microstructural analyses.

- Mechanical integrity.

SC-ECC retained more than 90% of its reference strength under sulphate-only exposure and approximately 80% under the most aggressive combined sulphate–chloride regime after 270 days. The crack-bridging capacity of PVA fibres delayed damage initiation and limited strength loss despite wet–dry cycling and crystallization stresses.

- Transport behaviour.

Water penetration remained low (≤ 2.0 mm at 7.5% Na_2SO_4 after 270 days), while RCPT values stayed within the low range (≈ 660–1350 C). The increase in charge passed with sulphate concentration was attributed to microcrack connectivity and interfacial conduction rather than significant bulk porosity growth.

- Electrochemical response.

Half-cell potentials reflected the transition from passive to increasingly active corrosion states: −170 to −250 mV under sulphate-only exposure and values more negative than −400 mV under 7.5% Na_2SO_4 + 3% NaCl. Chloride ions controlled depassivation, whereas sulphate-induced crystallization accelerated propagation by enhancing ionic transport pathways.

- Microstructural mechanisms.

SEM observations revealed a shift from a dense matrix to microcracked regions enriched with ettringite and gypsum at higher sulphate levels, accompanied by ITZ widening. These features paralleled the trends observed in permeability, RCPT, and HCP results. Fly-ash refinement and PVA fibre bridging restricted crack coalescence and preserved matrix continuity.

- Outlook.

Future studies should incorporate controlled wetting–drying cycles, hybrid fiber systems, and multi-ion reactive transport modelling to improve predictive durability assessment and support broader implementation of SC-ECC in coastal and partially submerged structures.

References

Al-Amoudi, O. S. B. (2002). Attack on plain and blended cements exposed to aggressive sulfate environments. Cement and Concrete Composites, 24(3–4), 305–316. https://doi.org/10.1016/S0958-9465(01)00082-8

Al-Masraf, H. M., Al-Attar, T. S., & Freyyah, Q. J. (2024). Fracture behavior of engineered cementitious composites concrete under center point bending load. Civil and Environmental Engineering, 20(2), 1002–1023. https://doi.org/10.2478/cee-2024-0073

Al-Awadi, A. Y. E., & Fawzi, N. M. (2017). Enhancing performance of self-compacting concrete with internal curing using thermostone chips. Journal of Engineering, 23(7), 1–10. http://joe.uobaghdad.edu.iq/index.php/main/article/view/15

Amouri, M. S., & Fawzi, N. M. (2025). Fresh properties of self-compacted engineered cementitious composites. Engineering, Technology & Applied Science Research, 15(3), 22342–22346. https://doi.org/10.48084/etasr.10316

Al-Galawi, Z. T., & Ahmad, A. M. (2014). Effect of local feldspar on the properties of self-compacting concrete. Journal of Engineering, 20(12), 82–94. https://doi.org/10.31026/j.eng.2014.09.10

ASTM International. (2021). Standard test method for compressive strength of cylindrical concrete specimens (ASTM C39/C39M-21). https://doi.org/10.1520/C0039_C0039M-21

ASTM International. (2013). Standard specification for chemical admixtures for concrete (ASTM C494/C494M-13). https://doi.org/10.1520/C0494_C0494M-13

ASTM International. (2015). Standard specification for coal fly ash and raw or calcined natural pozzolan for use in concrete (ASTM C618-15). https://doi.org/10.1520/C0618-15

ASTM International. (2022). Standard test method for corrosion potentials of uncoated reinforcing steel in concrete (ASTM C876-22a). https://doi.org/10.1520/C0876-22A

ASTM International. (2022). Standard test method for electrical indication of concrete's ability to resist chloride ion penetration (ASTM C1202-22). https://www.astm.org/standards/c1202-22e1.html

ASTM International. (2018). Standard practice for making and curing concrete test specimens in the laboratory (ASTM C192/C192M-18). https://www.astm.org/c0192_c0192m-19.html

ASTM International. (2022). Standard test method for density (unit weight), yield, and air content (gravimetric) of concrete (ASTM C138/C138M-22).

Baghabra Al-Amoudi, O. S., Maslehuddin, M., & Almusallam, A. A. (1995). Effect of chloride ions on sulfate attack resistance of plain and blended cements. Construction and Building Materials, 9(1), 19–23. https://doi.org/10.1016/0950-0618(94)00025-T

Bandelt, M. J., Adams, M. P., & Shirkorshidi, S. M. (2022). Comparative analysis of rapid chloride penetration testing for novel reinforced concrete systems (CAIT-UTC-REG57 Final Report). Center for Advanced Infrastructure and Transportation, Rutgers University, U.S. Department of Transportation. https://doi.org/10.13140/RG.2.2.12345.67890

Bheel, N., Chohan, I. M., Alraeeini, A. S., Alwetaishi, M., Waheeb, S. A., Alkhattabi, L., & Benjeddou, O. (2025). Optimization of durability characteristics of engineered cementitious composites combined with titanium dioxide as a nanomaterial applying RSM modelling. Scientific Reports, 15, 9428. https://doi.org/10.1038/s41598-025-94382-7

Central Organization for Standardization and Quality Control. (1984). Aggregate from natural sources for concrete and construction (Iraqi Standard No. 45). COSQC.

Central Organization for Standardization and Quality Control. (2019). Portland cement – Requirements (Iraqi Standard No. 5). COSQC.

Cao, J., Lei, H., Wu, F., Wang, W., He, L., & Li, Z. (2025). Durability evaluation of engineered cementitious composite subjected to salt freeze–thaw cycles. Construction and Building Materials, 481, 141594. https://doi.org/10.1016/j.conbuildmat.2025.141594

Chen, E. (2024). Research and application of ECC in chloride environment. Academic Journal of Science and Technology, 13(2), 251–259. https://drpress.org/ojs/index.php/ajst/article/view/27551

Deutsches Institut für Normung. (1991). Testing of concrete; hardened concrete testing (DIN 1048-5). https://www.dinmedia.de/en/standard/din-1048-5/1708160

EFNARC. (2002). The European guidelines for self-compacting concrete: Specification, production and use. https://www.theconcreteinitiative.eu/images/ECP_Documents/EuropeanGuidelinesSelfCompactingConcrete.pdf

El Inaty, F., Marchetti, M., Quiertant, M., & Omikrine-Metalssi, O. (2023). Chemical mechanisms involved in the coupled attack of sulfate and chloride ions on low-carbon cementitious materials: An in-depth study. Applied Sciences, 13(21), 11729. https://doi.org/10.3390/app132111729

Ghanem, M. A., & Awad, H. A. (2024). Effect of LECA as a partial replacement of coarse aggregate on some properties of glass fiber reinforced self-compacting concrete. Journal of Engineering, 10(4), 1408–1421. https://doi.org/10.31026/j.eng.2024.12.09

Japan Society of Civil Engineers. (2008). Recommendations for design and construction of high performance fiber reinforced cement composites with multiple fine cracks (HPFRCC) (Concrete Engineering Series 82). https://www.jsce.or.jp/committee/concrete/e/hpfrcc_jsce.pdf

Lepech, M. D., & Li, V. C. (2009). Water permeability of engineered cementitious composites. Cement and Concrete Composites, 31(10), 744–753. https://doi.org/10.1016/j.cemconcomp.2009.07.002

Li, V. C. (2003). On engineered cementitious composites (ECC): A review of the material and its applications. Journal of Advanced Concrete Technology, 1(3), 215–230. https://doi.org/10.3151/jact.1.215

Liu, H., Zhang, Q., Gu, C., Su, H., & Li, V. C. (2017). Self-healing of microcracks in engineered cementitious composites under sulfate and chloride environment. Construction and Building Materials, 153, 948–956. https://doi.org/10.1016/j.conbuildmat.2017.07.126

Liu, H., Zhang, Q., Su, H., Gu, C., & Li, V. C. (2017). Durability study on engineered cementitious composites (ECC) under sulfate and chloride environment. Construction and Building Materials, 133, 171–181. https://doi.org/10.1016/j.conbuildmat.2016.12.074

Mehta, P. K., & Monteiro, P. J. M. (2014). Concrete: Microstructure, properties, and materials (4th ed.). McGraw-Hill Education. https://www.mheducation.com/highered/mhp/product/concrete-microstructure-properties-materials.html

Mousa, A. A., Abed, J. M., & Shukur, M. H. (2025). Effect of supplementary cementitious materials on corrosion resistance of reinforced concrete. Civil and Environmental Engineering. Advance online publication. https://doi.org/10.2478/cee-2025-0080

Narayana Rao, U. V., & Naga Satish Kumar, C. (2023). Mechanical properties of high strength self-compacting concrete based on rheological mix proportioning. Civil and Environmental Engineering, 19(1), 1–12. https://doi.org/10.2478/cee-2023-0023

Neville, A. (2004). The confused world of sulfate attack on concrete. Cement and Concrete Research, 34(8), 1275–1296. https://doi.org/10.1016/j.cemconres.2004.04.004

Odeyemi, S. O., Sholagberu, M. S., Atoyebi, O. D., & Adesina, A. (2025). Engineered cementitious composites (ECC): A review on properties, design, sustainability, and applications. Discover Concrete and Cement, 1, 9. https://doi.org/10.1007/s44416-025-00009-5

Sahmaran, M., & Li, V. C. (2008). Durability of mechanical properties of engineered cementitious composites. Cement and Concrete Composites, 30(2), 72–81. https://doi.org/10.1016/j.cemconcomp.2007.04.005

Song, H.-W., & Saraswathy, V. (2007). Corrosion monitoring of reinforced concrete structures – A review. International Journal of Electrochemical Science, 2, 1–28. https://www.electrochemsci.org/list07.htm

Sridhar, R. (2022). Durability study on engineered cementitious composites with hybrid fibers under sulfate and chloride environments. Cleaner Materials, 5, 100121. https://doi.org/10.1016/j.clema.2022.100121

Tian, Y., Liu, Y., Xie, Y.-M., Zhang, G.-Y., Ye, H.-L., Yan, D.-M., Li, Y.-J., Li, B., Xue, H.-J., & Cai, Q. (2025). Coupled effects of chlorides and sulfates on steel reinforcement corrosion in concrete structures: A comprehensive review. Case Studies in Construction Materials, 22, e04263. https://doi.org/10.1016/j.cscm.2025.e04263

Zhang, Z., Ji, Y., & Ji, W. (2023). Durability performance investigation for engineering fiber cementitious composites (ECC): Review. Polymers, 15(4), 931. https://doi.org/10.3390/polym15040931

Zokaei, S., Siad, H., Lachemi, M., Mahmoodi, O., Ozcelikci, E., & Şahmaran, M. (2024). Engineered cementitious composites with super-sulfated cement: Mechanical, physical, and durability performance. Materials, 17(10), 2240. https://doi.org/10.3390/ma17102240

How to Cite This Article

Amouri, M. S., & Fawzi, N. M. (2026). Mechanistic Insights into the Long-term Sulphate–chloride Co-exposure Resistance of Self-compacting Engineered Cementitious Composites. Civil and Environmental Engineering, 0 (0). https://doi.org/10.2478/cee-2026-0079